Unveiling subsurface hydrogen-bond structure of hexagonal water ice

Yuji Otsuki,[1] Toshiki Sugimoto,[1,2,*] Tatsuya Ishiyama,[3] Akihiro Morita,[4,5] Kazuya Watanabe,[1] and Yoshiyasu Matsumoto[1,†]

[1]*Department of Chemistry, Graduate School of Science, Kyoto University, Kyoto 606–8502, Japan*

[2]*Precursory Research for Embryonic Science and Technology (PRESTO), Japan Science and Technology Agency (JST), Saitama 332-0012, Japan*

[3]*Department of Applied Chemistry, Graduate School of Science and Engineering, University of Toyama, Toyama 930–8555, Japan*

[4]*Department of Chemistry, Graduate School of Science, Tohoku University, Sendai 980–8578, Japan*

[5]*Elements Strategy Initiative for Catalysts and Batteries (ESICB), Kyoto University, Kyoto 615–8520, Japan*

(Received 13 March 2017; revised manuscript received 24 May 2017; published 5 September 2017)

The phase-resolved sum-frequency-generation (SFG) spectrum for the basal face of hexagonal ice is reported and is interpreted by molecular dynamics simulations combined with *ab initio* quantum calculations. Here, we demonstrate that the line shape of the SFG spectra of isotope-diluted OH chromophores is a sensitive indicator of structural rumpling uniquely emerging at the subsurface of hexagonal ice. In the outermost subsurface between the first (B1) and second (B2) bilayer, the hydrogen bond of O_{B1}-H $\cdots$ O_{B2} is weaker than that of O_{B1} $\cdots$ H-O_{B2}. This implies that subsurface O-O distance is laterally altered, depending on the direction of O-H bond along the surface normal: H-up or H-down, which is in stark contrast to bulk hydrogen bonds. This new finding uncovers how water molecules undercoordinated at the topmost surface influence on the subsurface structural rumpling associated with orientational frustration inherent in water ice.

DOI: 10.1103/PhysRevB.96.115405

I. INTRODUCTION

Water ice is one of the most abundant solid substances in nature and its surface plays crucial role in a variety of processes in physics, chemistry, and earth planetary science: surface premelting for unusual slipperiness in skating and skiing [1–4], sublimation and condensation in the atmospheric air and planetary systems [5,6], charge generation and separation in thunder cloud [7], heterogeneous reactions in the Earth's ozone layer and interstellar space [8–11], etc. Because ice is a hydrogen bonded aggregate of water molecules, its surface physicochemical properties are dominated not only by the lattice translational structure (position of oxygen atoms) but also by the sublattice structure (orientations of water molecules or configurations of hydrogen atoms) of ice surface [12,13].

The surface of a solid is not confined to its topmost layer, but consists of transition layers extending to the bulk, the subsurface. As a result of the abrupt truncation of materials, the lattice and electronic structures of surfaces generally differ from those of the bulk, which results in the unique physicochemical properties and heterogeneous processes of solid surfaces [14–16]. Thus structural relaxation and reconstruction at solid surfaces have been intensively studied by low energy electron diffraction, ion and x-ray scattering, and transmission electron microscopy [17–20]. Although these conventional analytical techniques have been successfully applied to strongly bonded materials, metals and semiconductors, they invasively probe fragile and insulating solid substances composed of soft molecular systems such as water ice [21–24].

The structure of bulk crystalline ice in the common paraelectric phase (hexagonal ice Ih) has been well known; a local tetrahedral configuration of hydrogen bonded water molecules is arranged so that every water molecule constitutes hexagonal bilayers, where molecular orientation is disordered and geometrically frustrated under the Bernal-Fowler-Pauling ice rules [1,25,26]: each pair of oxygen atoms holds one hydrogen atom and two hydrogen atoms are closely located at each oxygen atom (Fig. 1). In contrast, the surface structure of ice has been ill-characterized. Although molecular-level surface structural analysis techniques such as helium atom scattering and scanning probe microscopy [27–30] have demonstrated that the topmost basal surface of ice Ih(0001) is terminated with a full-bilayer structure [31,32] (Fig. 1), it has been extremely difficult to determine the structure of buried subsurfaces. In addition, the orientation of water molecules that are geometrically frustrated is extremely hard to investigate with traditional techniques because hydrogen has only a single electron and responds extremely weakly to the probes of the techniques. Thus the determination of the hydrogen-bond structure at an ice surface has been an experimental challenge.

Sum-frequency generation (SFG) vibrational spectroscopy has advantages over the conventional methods in investigating the structure of ice surface. The SFG process is noninvasive and can be surface sensitive because SFG processes are governed by the second-order nonlinear susceptibility $\chi^{(2)}$ that takes nonzero values in the media where three-dimensional lattice periodicity with inversion symmetry is broken [33,34]. Because the imaginary part of $\chi^{(2)}$ contains the information of molecular directional orientation, this method allows us to determine molecular orientations at ice surfaces if $\mathrm{Im}\chi^{(2)}$ is retrieved [35–39]: OH oscillators with H-up and H-down orientation show positive and negative signs, respectively, in an $\mathrm{Im}\chi^{(2)}$ spectrum of the hydrogen-bonded OH-stretch band. In spite of these advantages, previous SFG studies have suffered from two serious difficulties in determining the surface structure of crystalline ice [40–48]. All the SFG works have been conducted with homodyne detection [40–48]; SFG spectra are obtained through $|\chi^{(2)}|^2$, where the information of

*toshiki@kuchem.kyoto-u.ac.jp
†matsumoto@kuchem.kyoto-u.ac.jp

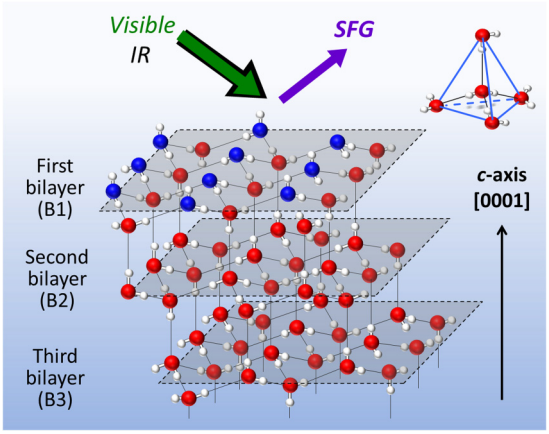

FIG. 1. Schematic illustration of an ideal full-bilayer termination structure of ice Ih(0001) surface among one of the many possible random orientational alignments of water that satisfies the ice rules. Oxygen of four-coordinated water molecules is colored by red, while that of three-coordinated water molecules at the topmost bilayer is colored by blue. For SFG vibrational spectroscopy, infrared and visible laser pulses are coaxially irradiated onto the ice Ih(0001) surface. (Inset) Schematic illustration of a local tetrahedral hydrogen-bond network.

H-up and H-down orientations is completely lost. Furthermore, they have targeted H_2O ice, where the hydrogen bonded OH-stretch bands are extremely complicated due to the strong inter- and intramolecular couplings [49–54] that delocalize vibrational wave functions among OH chromophores of several water molecules. This hampers the assignments of the OH-stretch bands in the SFG spectra of the previous studies [40–48]. Therefore the strong couplings in H_2O ice together with the inherent limitation of homodyne-detected $|\chi^{(2)}|^2$ SFG measurements in determining molecular orientations have impeded a detailed understanding of the hydrogen-bond structure at the ice surface [40–48].

To overcome these problems and exclude any possible structural deformation by impurities [2], we have challenged heterodyne-detected phase-resolved SFG vibrational spectroscopy for probing the basal (0001) face of isotope-diluted HDO ice Ih grown on Rh(111) substrate under ultrahigh-vacuum environment. In contrast to H_2O ice, inter- and intramolecular vibrational couplings are negligible in the isotope diluted HDO ice; this makes the hydrogen-bonded OH-stretch bands of ice very simple [35,55–59]. In the present study, a clear correlation between the peak wavenumber of the hydrogen-bonded OH stretch band of isotope diluted HDO ice and the intermolecular hydrogen-bond distance [57–59] is found, which enables us to investigate the structure of ice surface in terms of intermolecular distance and H-up/H-down orientation from the peak wavenumber and sign of the $\mathrm{Im}\chi^{(2)}$ spectra.

II. MATERIALS AND METHODS

A. Preparation of clean Rh(111) substrate

A single-crystal Rh(111) substrate was purchased from MaTeck GmbH. The Rh(111) single-crystal surface was cleaned by several cycles of Ar^+ bombardment at 1 keV and annealing at 1000 K in an ultrahigh vacuum (UHV) chamber at a base operating pressure below 3×10^{-8} Pa. The surface cleanliness and structure of the substrate were routinely checked by using low-energy electron diffraction (LEED), Auger-electron spectroscopy (AES), and temperature programmed desorption (TPD) of water [60–62].

B. Preparation of HDO source and H/D isotope ratio

Isotopically diluted HDO water was used because the spectra of the local OH-stretch bands are much simpler than those of H_2O [35,55,57,58]. D_2O water with an isotopic purity of 99.96 atom % D purchased from ISOTEC and H_2O (milli-Q) were mixed to obtain H diluted HDO water. HDO concentration in the D_2O-rich water vapor was estimated to be ~32 mol% ([OD]/[OH] ratio ~3.4) with a quadrupole mass spectrometer (QMS) [63] equipped with the UHV chamber [35,64–67]. The water samples were carefully pre-degassed in an ultrahigh-vacuum gas line by repeating freeze-pump-thaw cycles. The cleanliness of water vapor was also checked by QMS, which showed no appreciable signals derived from contaminants.

C. Preparation of (0001) surface of ice Ih

Ice Ih(0001) was grown in the UHV chamber by physical vapor deposition of isotope diluted HDO on Rh(111) at 145 K, where c axis is parallel to the surface normal [60,68,69]. The deposition rate was 0.01 bilayer/s; this is slow enough to grow crystalline ice instead of amorphous ice [10,70–72]. The amount of adsorbed water molecules is expressed in the bilayer unit (BL) following the previous studies of ice surfaces [28,52,70–75]; 1 BL corresponds to the amount of water molecules in a bilayer of bulk ice Ih($\sim 1.1 \times 10^{19}$ m^{-2}) [1], almost the same as the amount of water adsorbed in the first layer saturated on Rh(111) [69,76]. The conventional TPD technique was used for confirming the crystallinity [77] and cleanliness of the ice surface, and calibrating the amount of water molecules adsorbed on Rh(111) [60]. The main constituents of the residual gas in the UHV chamber and gas line is H_2 that does not adsorb on ice surface at our experimental temperature [10]. We have never observed any appreciable TPD signal, C-H stretch SFG spectrum, and frequency shift of free OD stretch SFG spectrum [78] derived from contaminants of ice surface.

D. SFG setup

Experiments were performed in the UHV chamber combined with an optical system for infrared-visible SFG spectroscopy that was described in detail elsewhere [35,64–67]. Briefly, the output pulse of a Ti:sapphire regenerative amplifier (Spectra physics, 1 kHz, ~2 mJ/pulse) was split into two to generate a narrow band 800-nm "visible" pulse (<1 μJ/pulse) and a broadband infrared pulse (150 fs duration, <5 μJ/pulse, centered at ~3260 cm^{-1}) that covers almost the entire range of the hydrogen bonded local OH stretching band of HDO crystalline ice. The homodyne- and heterodyne-detected *PPP*-SFG spectra (Figs. 2 and 3) and *SSP*-SFG spectra were measured with visible and infrared laser pulses coaxially aligned at

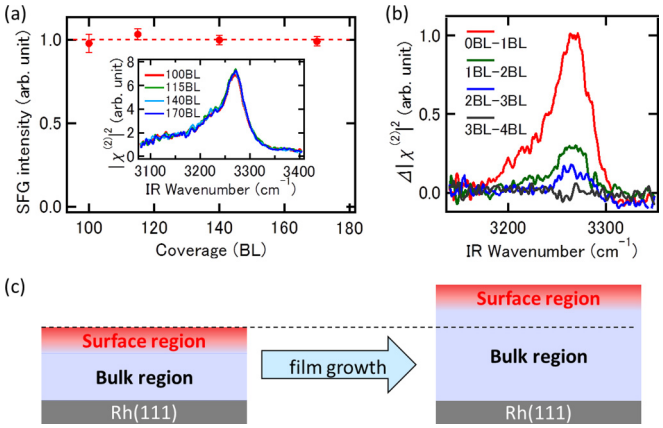

FIG. 2. (a) Thickness dependence of SFG intensity and (inset) $|\chi^{(2)}|^2$ spectra of the hydrogen-bonded OH stretching band of isotope diluted HDO ice-Ih(0001) film on Rh(111) measured at 120 K with *PPP* configuration. (b) D_2O-deposition-induced change of the $|\chi^{(2)}|^2$ spectra of the isotope diluted ice film with 140-bilayers thickness at 120 K. (c) Schematic illustration of increase of film thickness and the resultant conversion of surface region into bulk during the *layer-by-layer* growth mode.

an incident angle of 61.5°, where the coherence length is ∼4.7 μm. Each polarization is expressed in the sequence of SFG, visible, and infrared light and the Z axis of the lab flame is defined to be parallel to the c axis of ice Ih(0001). The phase of heterodyne signals was determined by referencing the free-OD stretch band as an internal reference (Appendix A). To avoid laser heating and damage of ice samples [41,43], the laser pulses were gently focused on sample surfaces; the spot size is ∼1 mm in diameter. Increase of sample temperature during SFG measurements was less than 1 K. The reproducibility of the SFG spectra with respect to the sample position and laser intensity [41,43,48] was carefully checked.

E. MD simulations and QM/MM calculations

The calculation of the structure of ice Ih was conducted using classical MD simulations. The methodology of QM/MM calculations combined with classical MD simulations for the orientationally disordered ice Ih surface is essentially same as the previous study [52,53]. Here, we summarize the present computational procedure briefly. The MD simulation was carried out in 3D periodic boundary conditions with the Ewald sum method. The TIP4P/Ice model [79], which has the melting point temperature of 272.2 K, was employed for an equilibration run as follows. An orientationally disordered ice Ih unit consisting of 1120 water molecules was prepared with the Monte Carlo method [80] in a rectangular simulation box with dimensions $L_X \times L_Y \times L_Z = 31.44$ Å $\times$ 31.11 Å $\times$ 40 Å. The system was equilibrated in an NPT ensemble during 1 ns to create a periodic structure of bulk ice Ih with stable local structure and volume, where the semi-isotropic pressure coupling (pressures in XY and Z couple separately) with $P = 1$ atm was applied by using the Parrinello-Rahaman barostat [81] and the temperature was kept at a desired one with the Nose-Hoover thermostat [82,83] (time step $\Delta t = 2.0$ fs, temperature T = 130 K) with GROMACS package (version 4.6.1) [84]. Further equilibration in the NVT ensemble was carried out for 10 ns, where L_Z is elongated to 150 Å, while the converged L_X and L_Y were fixed, generating an ice slab of 10 BL (∼34 Å) thickness with two basal plane surfaces normal to the Z axis.

After the equilibration run mentioned above, the flexible and polarizable point dipole (PD) model developed by us [85] was used to calculate the structure (Figs. 5, 11, and 12) and SFG vibrational spectra (Figs. 4 and S1) of ice Ih(0001)

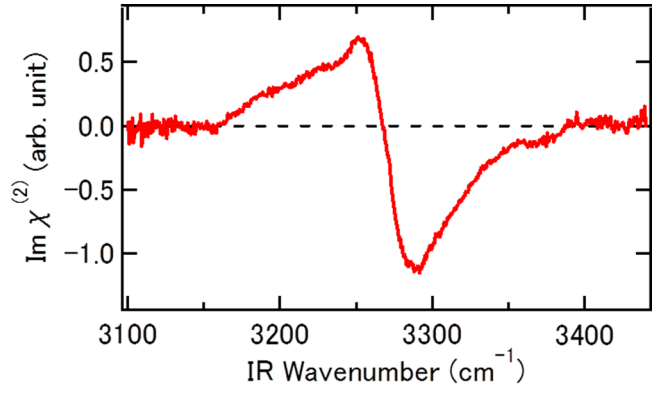

FIG. 3. The experimentally observed resonant Im$\chi^{(2)}$ spectrum for the hydrogen-bonded OH-stretching band of isotope diluted ice Ih(0001) measured at 120 K with *PPP* configuration. The spectrum is dominated by the *ZZZ*-component of $\chi^{(2)}$ (Appendix B).

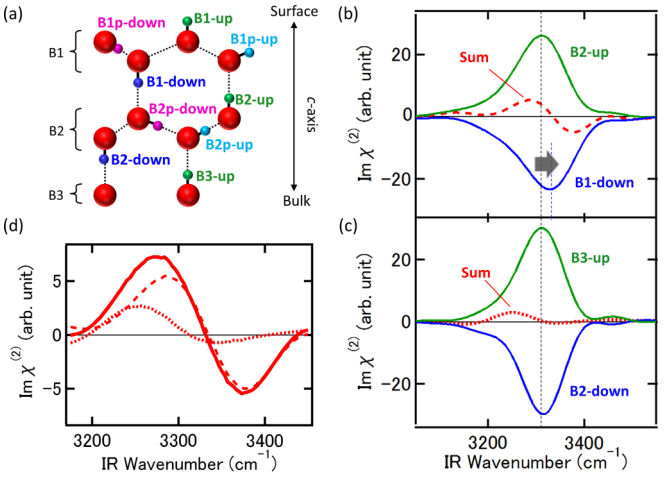

FIG. 4. (a) Classification of OH oscillators at the surface of ice Ih(0001). Only OH oscillators used for definition are shown here and oxygen atoms are colored by red. Bn indicates the nth bilayer from the topmost surface ($n = 1, 2, 3$), and Bn-up (green spheres) and Bn-down (blue spheres) are interbilayer OH bonds that orient parallel to the c axis and point toward the surface and into the bulk, respectively. *Bn*p-up (cyan spheres) and B*n*p-down (magenta spheres) are intrabilayer OH bonds that orient nearly perpendicular to the c axis and lean toward the surface and into the bulk, respectively. [(b)–(d)] The *ZZZ*-component of resonant Im$\chi^{(2)}$ spectra derived from the QM/MM calculation for the hydrogen-bonded OH-stretching mode of isotope-diluted ice Ih(0001). The spectra of Bn-down (blue), B($n + 1$)-up (green) and their sum [red, Bn-down +B($n + 1$)-up] for $n = 1$ (b) and $n = 2$ (c). The spectra of B1-down+B2-up (dashed), B2-down+B3-up (dotted), and their sum (solid) (d).

surfaces. After an additional short NVT ensemble simulation during 1 ps (time step $\Delta t = 0.61$ fs) for stabilization, the ensemble average of 10 ps per one MD trajectory was taken by NVE ensemble simulation in 256 parallel computations with different initial configurations, generating in total about 2.5 ns average for production run.

1. Extraction of structural information

First, the bilayer number n was assigned to all water molecules consisting of an ice slab by calculating the distance between the center of mass of the ice slab and for each water molecule, under the assumption that the bilayer thickness along the c axis is 3.66 Å. Next, a hydrogen-bond pair was found by the following geometric criteria: an H . . . O distance being below 2.5 Å and O-H . . . O angle (φ) being above 150°. If a H-bond donating water in Bn layer and an accepting water in B($n+1$) layer exist where the donating OH directs toward the bulk (i.e., $\cos\theta_{\mathrm{OH}}$ is negative, where θ_{OH} is an angle between an OH vector and the surface normal direction from bulk to surface), then we classified the donating water as Bn-down water [Fig. 4(a)]. Similarly, if a hydrogen-bond donating water in Bn layer and an accepting water in B(n-1) layer exist where the donating OH directs toward the surface, then we classified the donating water as Bn-up water [Fig. 4(a)]. Bnp-up (Bnp-down) water was defined if both donating and accepting waters exist in Bn layer and $\cos\theta_{\mathrm{OH}}$ becomes positive (negative) [Fig. 4(a)]. $R_{\mathrm{o\text{-}o}}$ and φ were sampled in every MD step for all hydrogen-bond pairs in each bilayer (Figs. 5, 11, and 12).

2. Spectral calculations

In the production run, QM/MM calculations to simulate SFG spectra were conducted (see also Sec. 2 of Ref. [86]), where a water cluster consisting of a central water molecule and surrounding D_2O molecules in the first solvation shell were treated as a QM region, while the other waters were treated as MM point charges [87]. The resonant ZZZ term of the second-order nonlinear susceptibility was calculated with the time correlation function formalism under the dipole approximation [88],

$$\chi^{(2)}_{R,ZZZ} = \frac{i\omega_{\mathrm{IR}}}{k_{\mathrm{B}}T}\int_0^{t_c} dt\, \exp(i\omega_{\mathrm{IR}}t)\langle A_{ZZ}(t)M_Z(0)\rangle, \quad (1)$$

where ω_{IR} is the infrared frequency, k_{B} is the Boltzmann constant, A and M are the polarizability and the dipole moment of the QM cluster, respectively. In each MD snapshot, we calculated the dipole moment and polarizability of the QM cluster by quantum chemical calculations, and we averaged the time correlation function of those quantities along with the MD trajectory [52]. The range of time integral t_c was set to 1.2 ps.

The QM calculations were performed with Hartree-Fock/6-31+G(d) under the electrostatic potential generated from the MM region [52,89]. The qualitative features of the spectra can be well reproduced even with the Hartree-Fock/6-31+G(d) basis set including double-zeta polarized functions and diffuse functions other than hydrogen atoms, because this basis set is capable of describing many-body polarization and charge transfer effects [52]; double-zeta polarized basis sets usually give correct qualitative information about IR intensity [90], inclusion of the diffuse function is essential for an accurate description of Raman spectra [91], and the diffuse function on hydrogen atoms has little effect on the molecular polarizability [92].

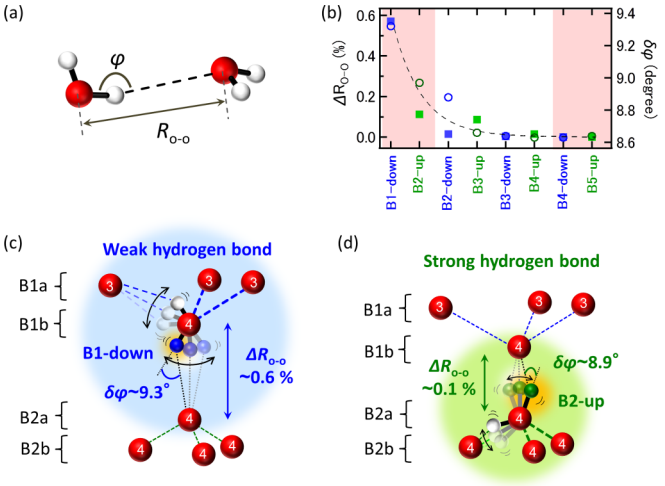

FIG. 5. (a) Schematic illustration of the intermolecular hydrogen bond. $R_{\mathrm{o\text{-}o}}$ is intermolecular distance and φ is O-H $\cdots$ O angle. (b) Structural parameters $\Delta R_{\mathrm{o\text{-}o}}$ (filled square) and $\delta\varphi$ (open circle) for interbilayer hydrogen bond calculated from the MD simulations. The black dashed line is guide to the eye. [(c) and (d)] Hydrogen-bond network at subsurface connected by water molecule with B1-down OH bond (c) and B2-up OH bond (d). Upper and lower halves of each bilayer are labelled with a and b, respectively. Hydrogen atoms in the intrabilayer hydrogen-bond network (colored dashed lines) in the B1 and B2 bilayer are omitted. The first solvation shell for water molecules with B1-down and B2-up OH bonds is marked with blue and green shadow, respectively, where the values of $\Delta R_{\mathrm{o\text{-}o}}$ and $\delta\varphi$ for the interbilayer hydrogen bond are also shown by colored characters. The white number written on the oxygen atom (red sphere) is coordination number of hydrogen bond for each molecule.

III. RESULTS AND DISCUSSION

A. Experimental results

Figure 2(a) shows the thickness dependence of $|\chi^{(2)}|^2$ SFG spectra of the hydrogen bonded OH-stretching band at 120 K with a PPP configuration. Both the amplitude and line shape of the band do not change with film thickness. It has been reported that the macroscopically continuous ice-Ih(0001) films with wide terraces more than $100 \times 100\,\mathrm{nm}^2$ are epitaxially grown on Rh(111) in the *layer-by-layer* growth mode at large thickness (more than ~100 bilayers) [28,30,68,69]. The spectral amplitude independent of the film thickness indicates that the ice film on Rh(111) is not ferroelectric [35].

For the paraelectric ice-Ih(0001) films on Rh(111), centrosymmetry is broken not only at the ice surface, i.e., vacuum/ice interface, but also at the ice/Rh(111) interface. Previous studies of STM and infrared spectroscopy reported that the hydrogen-bond network of one bilayer of ice on Rh(111) is similar to that of bulk ice Ih and the non-hydrogen-bonded H-down OH oscillators that directly interact with Rh atoms are significantly redshifted below 3100 cm^{-1} [60,69]. In good agreement with these results, we could not observe

any appreciable SFG spectra between 3150 and 3400 cm^{-1} during the deposition of few bilayers of the ice film. Therefore the observed SFG signal of the ice films on Rh(111) is derived from the ice surface, i.e., vacuum/ice interface.

Further evidence of the major contribution of ice surface to the SFG signal is that the SFG spectrum is diminished by additional deposition of pure-D_2O on the HDO ice-Ih(0001) surface; the SFG intensity of the OH-stretching band was steeply decreased by deposition of 1 bilayer of D_2O [Fig. 2(b)]. While the signal intensity was kept reduced by further deposition of D_2O, the amount of reduction per deposition layer was saturated at deposition of 3–4 bilayers of D_2O ice film [Fig. 2(b)]. This is because the deposition of additional ice bilayers converts the surface region of the original ice film into bulk [Fig. 2(c)] and the topmost D_2O ice on the HDO ice film does not possess a resonant SFG signal in the OH-stretching band. Therefore we can safely conclude that the observed SFG signal is mainly derived from the *electric-dipole* transition at the ice surface (Appendix C) and the SFG active layers are composed of about 3 bilayers at the top of the ice film, which supports the theoretically predicted structural fluctuation of ice-Ih(0001) surface [13].

Figure 3 shows an $\mathrm{Im}\chi^{(2)}$ spectrum of the hydrogen bonded OH-stretching band of the isotope diluted ice-Ih(0001) film with 140-bilayers thickness at 120 K. The spectrum is composed of two peaks with opposite signs: a positive peak at the lower wavenumber (∼3250 cm^{-1}) and a negative peak at the higher wavenumber (∼3290 cm^{-1}). The observed bipolar shape is quite different from the $\mathrm{Im}\chi^{(2)}$ spectra of isotope-diluted ice surface that were previously predicted from a model calculation [42] and the $\mathrm{Im}\chi^{(2)}$ spectrum of liquid water surface showing mainly a single negative peak [36–38]. The peak area of hydrogen-bonded OH-stretching band is more than one order of magnitude larger than that of dangling OH-stretching band (Appendix A), in good agreement with previous experimental and theoretical SFG studies [40,45,52]. The linewidth of the $|\chi^{(2)}|$ spectrum becomes sharper than that of the $\mathrm{Im}\chi^{(2)}$ spectrum (Fig. 7) due to complicated interference between the nonresonant constant originating from Rh(111) substrate and resonant signal from ice surface in the $|\chi^{(2)}|$ spectrum.

Note that the local electric-field components parallel to metal surface are substantially weakened even for the 140-BLs ice film on Rh(111) as a result of optical interference between incident and reflected light waves (Appendix B). Therefore the *PPP*-SFG signals from ice surface on metal substrate are dominated by the *ZZZ*-component of $\chi^{(2)}$ whereas the *SSP*-SFG signals were substantially small (Appendix B). As shown in Eq. (S10) in Sec. 3 of Ref. [86], the *ZZZ* component of $\chi^{(2)}$ is proportional to the additive sum of $\langle\cos\theta\rangle$ and $\langle\cos^3\theta\rangle$, where brackets indicate an ensemble average and θ is the polar angle of each OH oscillator with respect to the c axis (Fig. S2 in Ref. [86]). Therefore the SFG signal of OH oscillators nearly perpendicular to the c axis, i.e., the intrabilayer Bnp-up and Bnp-down OH defined in Fig. 4(a), is much weaker than that of OH oscillators parallel to the c axis, i.e., the interbilayer Bn-up and Bn-down OH [Fig. 4(a)]; the *ZZZ*-SFG signal of ice Ih(0001) is dominated by the OH oscillators parallel to the c axis. Note that the topmost B1-up OH oscillator, the so-called free-OH oscillator, does not form a hydrogen bond and shows the OH-stretching band around ∼3700 cm^{-1} [40,41]. Therefore the experimentally observed SFG spectra in the hydrogen-bonded OH-stretching region (Figs. 2 and 3) are derived from *hydrogen bonding interbilayer* OH oscillators at the subsurface. Because $|\chi^{(2)}|^2$ SFG intensity is substantially diminished by deposition of 1-bilayer D_2O ice [Fig. 2(b)], we can reasonably conclude that the positive and negative peaks in the $\mathrm{Im}\chi^{(2)}$ spectrum (Fig. 3) are dominated by the vibrational responses of B2-up and B1-down OH oscillators, respectively, at the outermost subsurface [Fig. 4(a)]. In general, as a hydrogen-bond connecting a neighboring molecule becomes stronger, the stretching frequency of the OH oscillator involved in the hydrogen bond decreases [55–59,93–95]. Therefore our result suggests that even in the same interbilayer between B1 and B2, the B1-down OH oscillators pointing toward the bulk form weaker hydrogen bonds than the B2-up OH oscillators pointing toward the surface. A difference in the wavenumber of 40 cm^{-1} suggests that the averaged O-H · · · O distance of an interbilayer connected by B1-down OH is ∼0.8% [57] longer than that connected by the B2-down OH.

B. Theoretical results

To elucidate the inequivalent hydrogen-bond length between B1 and B2 bilayers, we have conducted molecular dynamics (MD) simulations and quantum mechanical/molecular mechanical (QM/MM) spectral calculations, in which the effects of local field, polarization, and charge transfer at ice surface were explicitly taken into account [52,53]. Decomposing a calculated $\mathrm{Im}\chi^{(2)}$ spectrum into chromophores in each bilayer, we focus on interbilayer local-OH oscillators. Figure 4(b) shows that the calculated $\mathrm{Im}\chi^{(2)}$ spectra of B1-down and B2-up OH have opposite signs while their peaks are definitely shifted to each other; thus their sum results in a bipolar band [red dashed line in Figs. 4(b) and 4(d)]. Figure 4(c) shows that the B2-down and B3-up OH spectra have a similar trend as the B1-down and B2-up spectra, though the peak shift is much smaller. In this case, these two components largely cancel out each other. Therefore the net amplitude of the interbilayer OH spectra between B2 and B3 bilayers is smaller than that between B1 and B2 [Fig. 4(d)]. As going deeper into the bulk ($n \geqslant 3$), the contributions of interbilayer OH between Bn-down and B($n+1$)-up ($n \geqslant 3$) diminish and become negligibly small. In addition, the intrabilayer OH oscillators labelled Bnp-down/up in Fig. 4(a) are shown to have a minor contribution to the $\mathrm{Im}\chi^{(2)}$ spectrum because their amplitudes are about one order of magnitude smaller than those of the interbilayer OH oscillators (Sec. 2 of Ref. [86]). Therefore the bipolar band shape of the observed $\mathrm{Im}\chi^{(2)}$ spectrum (Fig. 3) is mainly attributed to the OH oscillators between the first and second bilayers in accordance with experimental results. Note that it is the large frequency difference between the interbilayer B1-down and B2-up OH bonds that makes these oscillators appreciable in the $\mathrm{Im}\chi^{(2)}$ spectrum [Figs. 4(b)–4(d)].

An interesting question arises: why are the stretching frequencies of OH chromophores in the interbilayer between the B1 and B2 bilayers are so different in comparison with interbilayers deep in the bulk? Because the O-H · · · O hydrogen-bonds connected by the Bn-down and B($n+1$)-up OH should be equivalent in the homogeneous bulk ice, this

question is pertinent to the unique character of subsurface environment. To answer this question, we examined systematically how the structure of each bilayer deviates from that of the bulk.

The structure of interbilayer hydrogen bonds is examined in terms of intermolecular distance ($R_{\text{o-o}}$) and O-H $\cdots$ O angle (φ) [Fig. 5(a)]. It is known that short $R_{\text{o-o}}$ and linear O-H $\cdots$ O alignment ($\varphi \sim 180^{\circ}$) are indicative of a strong hydrogen bond [57–59,93–97]. Figure 5(b) shows the half width at half maximum for the distribution of φ (Fig. 11), $\delta\varphi$, and deviations of $\langle R_{\text{O-O}}\rangle$ from the bulk value $\langle R^{\text{bulk}}_{\text{O-O}}\rangle$, $\Delta R_{\text{O-O}} = (\langle R_{\text{O-O}}\rangle - \langle R^{\text{bulk}}_{\text{o-o}}\rangle)/\langle R^{\text{bulk}}_{\text{O-O}}\rangle$, for various interbilayer OH bonds, where the brackets indicate ensemble average. As bilayers go deeper into the bulk, $\Delta R_{\text{o-o}}$ and $\delta\varphi$ converge to the bulk values irrespective of the orientation of the interbilayer OH bonds: $\Delta R_{\text{o-o}}$ and $\delta\varphi$ of B4-down OH bonds are the same with those of B5-up OH bonds [Fig. 5(b)]. In contrast, as bilayers get closer to the surface, $\Delta R_{\text{o-o}}$ and $\delta\varphi$ increase and become largest at the B1-B2 interbilayers. Moreover, they become dependent on the up/down orientation of OH bonds [Fig. 5(b)]; even in the same interbilayer, $\Delta R_{\text{o-o}}$ and $\delta\varphi$ of B1-down OH bonds are larger than those of B2-up OH bonds. This implies that the hydrogen-bond structure at the outermost subsurface is less ordered than bulk, which is in qualitative agreement with a previous report that demonstrated the broad distribution of water dipole moment in few bilayers of ice surface [13]. Due to the large mass of oxygen, the calculated values of $R_{\text{o-o}}$ would be hardly affected by nuclear quantum effects [98]. The deviations in $\langle R_{\text{O-O}}\rangle$ of the topmost interbilayer and intrabilayer, $\Delta R_{\text{o-o}} = +0.6\%$ and $+0.7\%$ [Figs. 5(c) and 11(b)], respectively, are much smaller than the $\sim$5.9% expansion at liquid-water surface [99] but almost the same with the $\sim$0.4% elongation at amorphous-ice surface [24], indicating that the hydrogen-bond network of liquid-water surface is considerably weaker than that at ice surfaces at low temperature.

Note that B1-down OH exhibits distinctively larger $\Delta R_{\text{o-o}}$ and $\delta\varphi$ than B2-up; the structure of interbilayer hydrogen bonds between the topmost bilayers markedly depends on the up/down orientation of OH bonds. Thus the equivalence of interbilayer hydrogen bond in the bulk is lost at the subsurface and the interbilayer structure is rumpled. The mechanism of interbilayer structural rumpling at the subsurface of ice-Ih(0001) is quite different from the traditionally proposed one at the subsurface of ionic insulator, where the displacement of less polarizable cations becomes larger than that of more polarizable anions due to the static local electric field at the surface [20]. As illustrated in Fig. 5(c), a water molecule with a B1-down OH in the B1b layer forms three hydrogen bonds with molecules in the topmost B1a layer, while water with a B2-up OH in the B2a layer is anchored by three hydrogen bonds with molecules in the deeper B2b layer [Fig. 5(d)]. The water molecules in the topmost B1a layer are three-coordinated while those in the subsurface B2b layer are four-coordinated. Therefore the intrabilayer hydrogen-bond network of B1 bilayer is more flexible and less ordered than that of B2 bilayer, which manifests itself in the differences in $\Delta R_{\text{o-o}}$ and $\delta\varphi$ of intrabilayer OH [Fig. 11(b)], and tetrahedrality [Fig. 12(b)]. As a consequence of larger librational fluctuation of water molecules in the B1 bilayer [$\delta\varphi \sim 9.8^{\circ}$, Fig. 11(b)] than in the B2 bilayer [$\delta\varphi \sim 8.8^{\circ}$, Fig. 11(b)], interbilayer hydrogen bonds connected by B1-down OH experience larger distortion [$\delta\varphi \sim 9.3^{\circ}$, Figs. 5(b) and 5(c)] than those with B2-up OH [$\delta\varphi \sim 8.9^{\circ}$, Figs. 5(b) and 5(d)]. The strain inequivalently weakens subsurface interbilayer hydrogen bonds, depending on the down/up orientation of OH bond, which results in the pronounced increase of the average value of $R_{\text{o-o}}$ [Fig. 5(b)] and the blue shift in the B1-down OH-stretch band [Fig. 4(b)]. This structural inequivalence is the origin of the bipolar band shape of the $\text{Im}\chi^{(2)}$ spectrum [Figs. 3 and 4(d)].

Cooperative many-body nature of hydrogen bond [96,97] would also contribute to the asymmetric interbilayer structure. As the strength of hydrogen bond increases, the water molecules involved in the hydrogen bond are more significantly polarized [13,93–97,100]. Therefore the B2-up OH of water in the strongly hydrogen-bonded B2 bilayer could more strongly donate a hydrogen in the interbilayer $O_{B1} \cdots$ H-O_{B2} hydrogen bond than the B1-down OH of water in the weakly H-bonded B1 bilayer. Indeed, we confirmed in the MD simulations that the difference of $\Delta R_{\text{o-o}}$ between the B1-down (O_{B1}-H $\cdots$ O_{B2}) and B2-up ($O_{B1} \cdots$ H-O_{B2}) hydrogen bonds in a nonpolarizable water model (TIP4P/Ice model) was about half of that in the polarizable water mode (point dipole model) shown in Fig. 5. This result suggests that the cooperative effect of hydrogen bond also contributes to the structural inequivalence and the bipolar band shape of the $\text{Im}\chi^{(2)}$ spectrum [Figs. 3 and 4(d)].

IV. CONCLUSIONS

In summary, we have succeeded in experimentally demonstrating for the first time the unique structural relaxation at a buried subsurface of insulating soft molecular solid, hexagonal water ice. The structural asymmetry of subsurface hydrogen bond (O_{B1}-H $\cdots$ O_{B2} and $O_{B1} \cdots$ H-O_{B2}) at ice-Ih(0001) was unveiled by means of the noninvasive phase-resolved SFG vibrational spectroscopy using heterodyne detection. The MD simulations and QM/MM spectral calculations described the peculiar features of experimentally observed $\text{Im}\chi^{(2)}$ spectrum (Fig. 3): the bipolar spectral shape and strong intensity of the hydrogen-bonded OH-stretching band in comparison to the free-OH-stretching band. The mean lattice relaxation of the order of $+0.6\% - 0.8\%$ in the outermost interbilayer is almost of the same extent as those of typical close-packed faces of simple and transition metals: Al($+0.9\%$), Cu(-0.7%), Pt($+1.0\%$), and Ir(-0.7%) [17,101]. These metals show homogeneous expansion or contraction of the subsurface interlayer spacing. In contrast, the structure of ice subsurface is rumpled: the outermost interbilayer lattice spacing of ice Ih(0001) is unequally expanded, depending on the up/down orientation of interbilayer OH bonds, because the amplitude of thermal librational fluctuations of water molecules with B1-down OH and B2-up OH is different [Figs. 5(c) and 5(d)]. This disparity is a manifestation of the difference of *intrabilayer* hydrogen-bond environment of B1b water from that of B2b water: B1b water is connected by three-coordinated B1a molecules, while B2a water is connected by four-coordinated B2b molecules. Although the possibility of proton-ordered Fletcher's striped structure at the topmost B1a layer [27,102] would affect the intrabilayer hydrogen-bond structure between

B1a and B1b layers [44,54], the deeper subsurface structure between B1b and B2a layers [Figs. 3 and 4] would be less sensitive to the topmost structure; whether or not ice-Ih (0001) has the Fletcher's striped phase [27,102,103] would not affect our main conclusions. Therefore geometrically frustrated H-up/H-down orientational disorder inherent in water ice [1,25,26] makes lattice and electronic structures at subsurface more inhomogeneous than they have ever been expected in the previous experimental studies [23,24,27–32] based on the classical Kossel picture of crystals. Note that these structural relaxations are observed at 120 K, which is much lower than the onset temperature of surface premelting (∼200 K) [40,41,48] and around the lower limit of the temperature range of the earth's atmosphere. Because crystalline ice is abundant in the temperature range below 200 K in the earth's atmosphere and in space, the structural rumpling associated with the orientational disorder would play key roles in a variety of anomalous physical and chemical properties of ice surface in nature [1–13] including mechanical friction, conduction of electrons, protons, and ions, energy transfer, and catalysis particularly relevant to astrophysics and atmospheric physical chemistry.

Note added in proof. Recently, we became aware of a related work by Smit *et al.* [104], reporting heterodyne-detected SFG spectra of H2O ice Ih(0001). They assumed that the dispersive shape of the main Im[chi2] band is indicative of quadrupole response. As discussed in Appendix C, however, Fig. 2 indicates that the contribution of the quadrupole response is negligibly small in the case of HDO ice Ih(0001). The present MD calculation elucidates the dispersive line shape (Fig. 3) with opposite bilayer-stitching OH vibrations between top two bilayers (Figs. 4 and 5). Disappearance of the dispersive line shape at around 3100 cm^{-1} above 200 K (Fig. 3 in Ref. [104]) implies that the dispersive band I of H2O ice Ih(0001) would not be derived from the bulk quadrupole response.

ACKNOWLEDGMENTS

We are grateful to N. Aiga, K. Harada, F. Kato, T. Hama, and H. Kato for fruitful discussions. This work was supported by MEXT KAKENHI: Grant-in-Aid for Scientific Research on Innovative Areas, Nos. 16H00937 and 25104003; JSPS KAKENHI Grant-in-Aid for Young Scientists (A), No. 16H06029; Grant-in-Aid for Scientific Research (A), No. 16H02249; Grants-in-Aid for Scientific Research (B) No. 16H04095; Grant-in-Aid for JSPS Research Fellow No. 17J08352. The computations were performed using Supercomputer Center of the Institute for Solid State Physics, the University of Tokyo, and Research Center for Computational Science, Okazaki, Japan.

The authors declare no competing financial interests.

APPENDIX A: EXTRACTION OF $\chi_R^{(2)}$ SPECTRA FROM PHASE-SENSITIVE SFG

We describe how to extract information on net orientation of OH oscillators from observed SFG signals. In our experimental condition, $\chi^{(2)}_{\mathrm{eff},PPP}$ is given in Eq. (S7) in Sec. 3 of Ref. [86]: $\chi^{(2)}_{\mathrm{eff},PPP} = T_Z^{\mathrm{SF}} T_Z^{\mathrm{VIS}} T_Z^{\mathrm{IR}} \chi^{(2)}_{ZZZ}$, where T_Z^{SF}, T_Z^{VIS}, and T_Z^{IR} are the transfer coefficients of sum-frequency, visible and infrared light, respectively; $\chi^{(2)}_{IJK}$ is the second-order nonlinear susceptibility. In the case of the HDO ice films on Rh(111), dependence of the transfer coefficients on the frequency of SF, visible and IR lights, is shown to be negligibly small (Appendix B). Thus $\chi^{(2)}_{\mathrm{eff},PPP}$ is approximated as

$$\begin{aligned}\chi^{(2)}_{\mathrm{eff},PPP}(\omega_{IR}) &= T\ \chi^{(2)}_{ZZZ}(\omega_{IR}) \\ &= |T| \exp(i\delta_T)\ \chi^{(2)}_{ZZZ}(\omega_{IR}) \\ &\propto \exp(i\delta_T)\ \chi^{(2)}_{ZZZ}(\omega_{IR}), \end{aligned} \tag{A1}$$

$$T \equiv T_Z^{\mathrm{SF}} T_Z^{\mathrm{VIS}} T_Z^{\mathrm{IR}} = |T| \exp(i\delta_T) \approx \text{const.}, \tag{A2}$$

where T is a product of transfer coefficients and δ_T is a phase of T. To obtain δ_T, we have used the free-OD stretch band as an internal reference. Because the free-OD oscillators at the topmost surface of HDO crystalline ice point toward the vacuum along the surface normal [35,40,41,78], δ_T can be determined under the assumption that the line shape of the $\mathrm{Im}\chi^{(2)}_{ZZZ}$ spectrum is well approximated by a Lorentzian function with positive sign (Fig. 6) [35,65]. Thus $\chi^{(2)}_{\mathrm{eff},PPP}$ multiplied by $\exp(-i\delta_T)$ gives $\chi^{(2)}_{ZZZ}$ for the hydrogen-bonded-OH stretch band (Fig. 7). Because the nonresonant term $\chi^{(2)}_{NR,ZZZ}$ is almost independent of the frequency of the incident infrared light [105,106], we can regard $\chi^{(2)}_{NR,ZZZ}$ to be constant and obtain the resonant term of $\chi^{(2)}_{R,ZZZ}$ as follows:

$$\chi^{(2)}_{R,ZZZ}(\omega_{IR}) = \chi^{(2)}_{ZZZ}(\omega_{IR}) - \chi^{(2)}_{NR,ZZZ}. \tag{A3}$$

A slight contribution of the nonresonant constant originating from Rh(111) substrate [107] appears in the $\mathrm{Im}\chi^{(2)}_{ZZZ}$ spectra as shown in Figs. 6(a) and 7(a). Note that the $\mathrm{Im}\chi^{(2)}_{R,ZZZ}$ spectrum shown in Fig. 3 was derived from the spectrum in Fig. 7(a) by subtracting the nonresonant background. Because

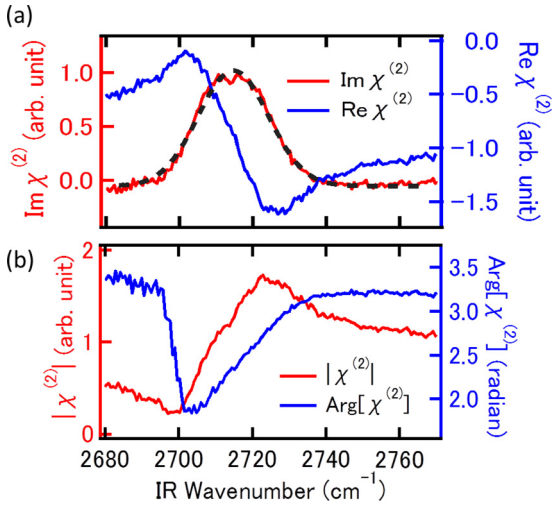

FIG. 6. (a) $\mathrm{Im}\chi^{(2)}_{ZZZ}$, $\mathrm{Re}\chi^{(2)}_{ZZZ}$ and (b) $|\chi^{(2)}_{ZZZ}|$ and $\mathrm{Arg}\chi^{(2)}_{ZZZ}$ spectra of the dangling OD-stretching band of HDO ice surface at 120 K. The HDO concentration in D_2O-rich water vapor was ∼32 mol%, corresponding to an [OD]/[OH] ratio of ∼3.4. A black dashed line is a result of curve fitting with a Lorentz function.

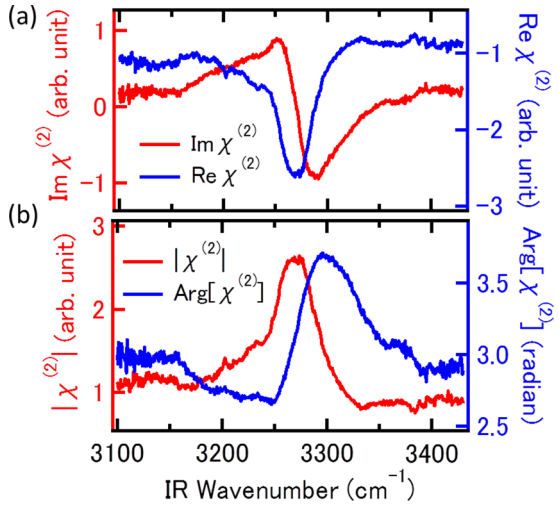

FIG. 7. (a) $\mathrm{Im}\chi^{(2)}_{ZZZ}$, $\mathrm{Re}\chi^{(2)}_{ZZZ}$ and (b)$|\chi^{(2)}_{ZZZ}|$ and $\mathrm{Arg}\chi^{(2)}_{ZZZ}$ spectra of the hydrogen-bonded OH-stretch band of HDO ice surface at 120 K. The HDO concentration in D_2O-rich water vapor was ∼32 mol%, corresponding to an [OD]/[OH] ratio of ∼3.4.

the scaling factor of the vertical axes of the $\mathrm{Im}\chi^{(2)}_{ZZZ}$ and $|\chi^{(2)}_{ZZZ}|$ spectra in Fig. 6 is the same as in Fig. 7 and the [OH]/[OD] ratio is about 1/3.4 in our HDO ice sample, the peak area of the hydrogen-bonded OH-stretching band is estimated to be more than one order of magnitude larger than that of the dangling OH-stretching band.

APPENDIX B: POLARIZATION AND FREQUENCY DEPENDENCE OF TRANSFER COEFFICIENTS

1. Transfer coefficients of *XXZ*, *YYZ*, and *ZZZ* polarization combinations

The electric field of sum-frequency light E^{SF} is given by the second-order nonlinear polarization P^{SF} multiplied by the output transfer coefficient T^{SF}:

$$E_I^{\mathrm{SF}} = T_I^{\mathrm{SF}} P_I^{\mathrm{SF}} \quad (I = X,Y,Z). \tag{B1}$$

The nonlinear polarization P^{SF} is induced by the local electric fields of input IR and visible light,

$$P_I^{\mathrm{SF}} = \chi^{(2)}_{IJK} E_J^{\mathrm{Vis,\,local}} E_K^{\mathrm{IR,\,local}} \quad (I,J,K = X,Y,Z). \tag{B2}$$

The local electric fields, which are applied to the molecules at a vacuum/ice interface, are composed of input electric fields (E^{IR} and E^{Vis}) and the input transfer coefficients (T^{IR} and T^{Vis}),

$$E_I^{\mathrm{Vis/IR,\,local}} = T_I^{\mathrm{Vis/IR}} E_I^{\mathrm{Vis/IR}}. \tag{B3}$$

When the visible and infrared light are collinearly irradiated under a nonresonant condition of visible light with respect to an electronic transition, the electric fields observed in the *PPP* and *SSP* polarization combination are

$$E_P^{\mathrm{SF}} = T_X^{\mathrm{SF}} T_X^{\mathrm{Vis}} T_Z^{\mathrm{IR}} \chi^{(2)}_{XXZ} E_X^{\mathrm{Vis}} E_Z^{\mathrm{IR}} + T_Z^{\mathrm{SF}} T_Z^{\mathrm{Vis}} T_Z^{\mathrm{IR}} \chi^{(2)}_{ZZZ} E_Z^{\mathrm{Vis}} E_Z^{\mathrm{IR}}, \tag{B4}$$

$$E_S^{\mathrm{SF}} = T_Y^{\mathrm{SF}} T_Y^{\mathrm{Vis}} T_Z^{\mathrm{IR}} \chi^{(2)}_{YYZ} E_Y^{\mathrm{Vis}} E_Z^{\mathrm{IR}}. \tag{B5}$$

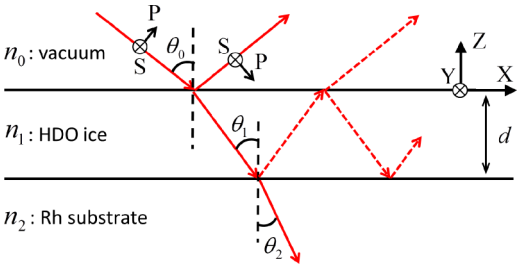

FIG. 8. Three-layer model under the infinite plane-wave approximation [108]. $n_m (m = 0,1,2)$ are the refractive indices of vacuum, HDO crystalline ice, and Rh(111) substrate, d is the thickness of HDO-ice layer. The direction of P-polarization vector of reflected light is the same as in Ref. [108]. The SFG process is assumed to take place at vacuum/ice interface.

Because we could not observe any appreciable SFG signals derived from the ice/Rh interface for sub-BL and few BLs thick ice films on Rh(111), we can reasonably assume that the SFG process takes place effectively only at the ice/vacuum interface. In the three-layer model shown in Fig. 8, the transfer coefficients are given as follows [108]:

$$T_Z^{\mathrm{IR}} = \sin\theta_0 \left(\frac{n_0}{\bar{n}}\right)^2 \left(1 - r^P_{1,2}\right) \frac{\exp(-i\phi) - r^P_{0,1}\exp(i\phi)}{\exp(-i\phi) + r^P_{0,1} r^P_{1,2}\exp(i\phi)}, \tag{B6}$$

$$T_X^{\mathrm{VIS}} = \cos\theta_0 \left(1 + r^P_{1,2}\right) \frac{\exp(-i\phi) + r^P_{0,1}\exp(i\phi)}{\exp(-i\phi) + r^P_{0,1} r^P_{1,2}\exp(i\phi)}, \tag{B7}$$

$$T_Y^{\mathrm{VIS}} = \left(1 + r^S_{1,2}\right) \frac{\exp(-i\phi) + r^S_{0,1}\exp(i\phi)}{\exp(-i\phi) + r^S_{0,1} r^S_{1,2}\exp(i\phi)}, \tag{B8}$$

$$T_Z^{\mathrm{VIS}} = \sin\theta_0 \left(\frac{n_0}{\bar{n}}\right)^2 \left(1 - r^P_{1,2}\right) \frac{\exp(-i\phi) - r^P_{0,1}\exp(i\phi)}{\exp(-i\phi) + r^P_{0,1} r^P_{1,2}\exp(i\phi)}, \tag{B9}$$

$$T_X^{\mathrm{SF}} = \left(1 + r^P_{0,1}\right) \left[\frac{i2\pi\sec\theta_0}{c\lambda_0 n_0} \cos\theta_0 + \frac{i2\pi\sec\theta_1}{c\lambda_0 n_1} \frac{r^P_{1,2} t^P_{1,0}\exp(2i\phi)}{1 - r^P_{1,0} r^P_{1,2}\exp(2i\phi)} \cos\theta_1 \right], \tag{B10}$$

$$T_Y^{\mathrm{SF}} = \left(1 + r^S_{0,1}\right) \left[\frac{i2\pi\sec\theta_0}{c\lambda_0 n_0} + \frac{i2\pi\sec\theta_1}{c\lambda_0 n_1} \times \frac{r^S_{1,2} t^S_{1,0}\exp(2i\phi)}{1 - r^S_{1,0} r^S_{1,2}\exp(2i\phi)} \right], \tag{B11}$$

$$T_Z^{\mathrm{SF}} = \left(1 - r^P_{0,1}\right) \left[\frac{i2\pi\sec\theta_0}{c\lambda_0 n_0} \left(\frac{n_1}{\bar{n}}\right)^2 \sin\theta_0 - \frac{i2\pi\sec\theta_1}{c\lambda_0 n_1} \times \frac{r^P_{1,2} t^P_{1,0}\exp(2i\phi)}{1 - r^P_{1,0} r^P_{1,2}\exp(2i\phi)} \left(\frac{n_0}{\bar{n}}\right)^2 \sin\theta_1 \right], \tag{B12}$$

$$\bar{n} = \sqrt{\frac{n_0^2 + n_1^2 + 4}{2\left(n_0^{-2} + n_1^{-2} + 1\right)}}, \tag{B13}$$

$$\phi = \frac{2\pi n_1}{\lambda} d\cos\theta_1, \tag{B14}$$

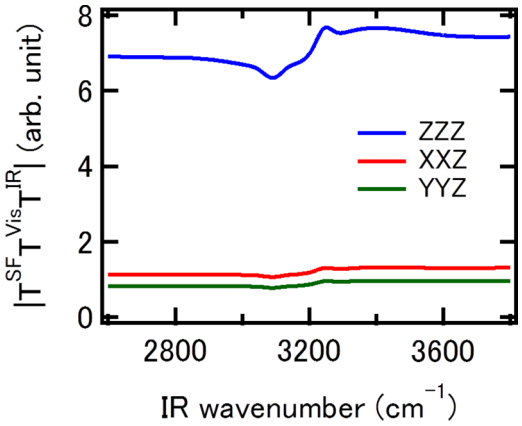

FIG. 9. IR wavenumber dependence of the transfer coefficients $|T_I^{\mathrm{SF}} T_I^{\mathrm{VIS}} T_Z^{\mathrm{IR}}|$ for $I = X, Y, Z$ simulated at $d = 51.8\,\mathrm{nm}$ (∼140 BL) and $\theta_0^{\mathrm{SF}} = \theta_0^{\mathrm{Vis}} = \theta_0^{\mathrm{IR}} = 61.5^\circ$.

$$r^P_{m-1,m} = \frac{n_{m-1}\cos\theta_m - n_m\cos\theta_{m-1}}{n_{m-1}\cos\theta_m + n_m\cos\theta_{m-1}}, \tag{B15}$$

$$r^S_{m-1,m} = \frac{n_{m-1}\cos\theta_{m-1} - n_m\cos\theta_m}{n_{m-1}\cos\theta_{m-1} + n_m\cos\theta_m}, \tag{B16}$$

$$t^P_{m-1,m} = \frac{2n_{m-1}\cos\theta_{m-1}}{n_{m-1}\cos\theta_m + n_m\cos\theta_{m-1}}, \tag{B17}$$

$$t^S_{m-1,m} = \frac{2n_{m-1}\cos\theta_{m-1}}{n_{m-1}\cos\theta_{m-1} + n_m\cos\theta_m}, \tag{B18}$$

where $\bar{n}$ is the refractive index at the interface between vacuum and HDO ice layer [109]; ϕ is the spatial phase offset accumulated by traversing an HDO ice layer, $r^{P/S}_{m-1,m}$ and $t^{P/S}_{m-1,m}$ are the amplitudes of reflection and transmission coefficients for P or S polarized light at the interface between m-1 and mth layers; n_0, n_1, and n_2 are the refractive indices of vacuum, HDO ice and Rh layer, respectively [107]. The refractive index of HDO ice n_1 was approximated with a linear combination of those of H_2O and D_2O ice [110] at a D_2O/H_2O mixing ratio of ∼3.4.

The input transfer coefficients T^{IR} and T^{Vis} are composed of a linear Fresnel factor and the projection factors of S *or* P component of incident light on to the X, Y, Z laboratory coordinate system, while the output transfer coefficient T^{SF} is composed of linear Fresnel factors, the projection factors, and the coefficients resulting from radiation of fields at the vacuum/ice interface: $\frac{i2\pi\sec\theta_0}{c\lambda_0 n_0}$ and $\frac{i2\pi\sec\theta_1}{c\lambda_0 n_1}$.

The products of transfer coefficients $T_I^{\mathrm{SF}} T_I^{\mathrm{VIS}} T_Z^{\mathrm{IR}}$ of various polarization combinations ($I = X, Y, Z$) are shown as a function of IR wavenumber in Fig. 9. The product of transfer coefficients of ZZZ polarization combination is about six times larger than that of XXZ polarization combination ($|T_Z^{\mathrm{SF}} T_Z^{\mathrm{VIS}} T_Z^{\mathrm{IR}} / T_X^{\mathrm{SF}} T_X^{\mathrm{VIS}} T_Z^{\mathrm{IR}}| \sim 6$), indicating that E_P^{SF} is dominated by the $\chi^{(2)}_{ZZZ}$ term in Eq. (B4).

The difference in the magnitude of SFG signals between XXZ and ZZZ polarization combinations originates from the polarization dependence of transfer coefficients of visible and sum-frequency light as follows. Because the reflection coefficient of visible light at the vacuum/ice interface is very small ($|r^P_{0,1}| \ll 1$), the transfer coefficients of visible light and their ratio are approximately expressed as

$$T_X^{\mathrm{VIS}} \approx \cos\theta_0\left(1 + r^P_{1,2}\right), \tag{B19}$$

$$T_Z^{\mathrm{VIS}} \approx \sin\theta_0\left(\frac{n_0}{\bar{n}}\right)^2\left(1 - r^P_{1,2}\right), \tag{B20}$$

$$\frac{T_Z^{\mathrm{VIS}}}{T_X^{\mathrm{VIS}}} \approx \tan\theta_0\left(\frac{n_0}{\bar{n}}\right)^2 \frac{1 - r^P_{1,2}}{1 + r^P_{1,2}}. \tag{B21}$$

Visible light is reflected at the ice/Rh interface with $r^P_{1,2} \sim -1$. Thus the $|T_Z^{\mathrm{VIS}}/T_X^{\mathrm{VIS}}|$ ratio becomes much larger than unity mainly due to the term derived from the Fresnel factors. Similarly, in the case of $\theta_0^{\mathrm{SF}} = \theta_0^{\mathrm{Vis}} = \theta_0^{\mathrm{IR}}$, $\bar{n} \sim n_1 > n_0$ $|r^P_{0,1}| \ll 1$ and $d/\lambda \ll 1$, the transfer coefficients of sum-frequency light are roughly approximated as

$$T_X^{\mathrm{SF}} \approx \frac{i2\pi\sec\theta_0}{c\lambda_0 n_0}\left(1 + r^P_{1,2}t^P_{1,0}\left(\frac{n_0}{\bar{n}}\right)^2\right)\cos\theta_0, \tag{B22}$$

$$T_Z^{\mathrm{SF}} \approx \frac{i2\pi\sec\theta_0}{c\lambda_0 n_0}\left(1 - r^P_{1,2}t^P_{1,0}\right)\sin\theta_0, \tag{B23}$$

$$\frac{T_Z^{\mathrm{SF}}}{T_X^{\mathrm{SF}}} \approx \tan\theta_0 \frac{1 - r^P_{1,2}t^P_{1,0}}{1 + r^P_{1,2}t^P_{1,0}}\left(\frac{n_0}{\bar{n}}\right)^2. \tag{B24}$$

Because the sum-frequency light in the visible spectrum is also reflected at the ice/Rh interface with $r^P_{1,2} \sim -1$ and transmitted at the ice/vacuum interface with $t^P_{1,0} \sim 0.8$, the $|T_Z^{\mathrm{SF}}/T_X^{\mathrm{SF}}|$ ratio becomes larger than unity: $|T_Z^{\mathrm{SF}}/T_X^{\mathrm{SF}}| \sim 1.5$ in our experimental condition. Therefore $|T_Z^{\mathrm{SF}} T_Z^{\mathrm{VIS}} T_Z^{\mathrm{IR}}|$ is much larger than $|T_X^{\mathrm{SF}} T_X^{\mathrm{VIS}} T_Z^{\mathrm{IR}}|$ (Fig. 9) mainly due to the polarization dependence of T^{VIS}.

We observed that $|\chi^{(2)}_{\mathrm{eff},SSP}|^2$ of ice films ($d \leqslant 140\,\mathrm{BL}$) on Rh(111) is much smaller than $|\chi^{(2)}_{\mathrm{eff},PPP}|^2$. This is due to the result shown in Fig. 9

$$\left|\frac{T_Y^{\mathrm{SF}} T_Y^{\mathrm{VIS}} T_Z^{\mathrm{IR}}}{T_Z^{\mathrm{SF}} T_Z^{\mathrm{VIS}} T_Z^{\mathrm{IR}}}\right|^2 \sim \left(\frac{1}{8}\right)^2, \tag{B25}$$

which is derived from the reflection properties of visible light at ice/Rh interface ($r^P_{1,2} \cong -1$ and $r^S_{1,2} \cong -1$) in the following equation:

$$\left|\frac{T_Y^{\mathrm{SF}} T_Y^{\mathrm{VIS}} T_Z^{\mathrm{IR}}}{T_Z^{\mathrm{SF}} T_Z^{\mathrm{VIS}} T_Z^{\mathrm{IR}}}\right|^2 \approx \left|\frac{T_Y^{\mathrm{VIS}}}{T_Z^{\mathrm{VIS}}}\right|^2 \approx \frac{1}{\sin\theta_0}\left(\frac{\bar{n}}{n_0}\right)^2 \frac{1 + r^S_{1,2}}{1 - r^P_{1,2}}. \tag{B26}$$

These results clearly indicate that the transfer (Fresnel) coefficients of ice films on a metal substrate are dominated by the reflection properties of visible light at ice/metal interface ($r^{P/S}_{1,2}$). Therefore, even for the SFG process taking place at the surface of ice with ∼100 BL thicknesses, the metal substrate can effectively suppress the electric-field components parallel to the metal surface as a result of the interference between incident and reflected light.

Figure 10 shows the amplitude and phase for the calculated transfer coefficients (T_Z^{IR} and T_Z^{SF}) and the experimentally observed $\chi^{(2)}_{\mathrm{eff},PPP}$ spectrum as a function of IR frequency.

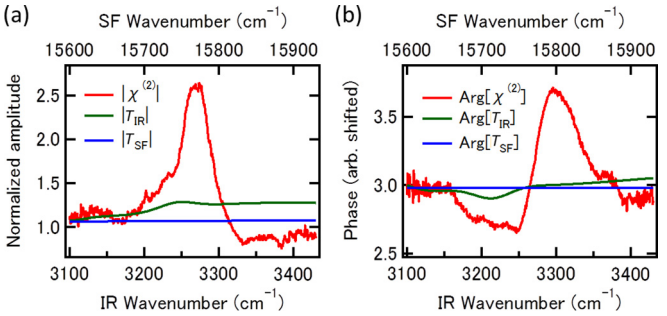

FIG. 10. IR wavenumber dependence of (a) amplitude and (b) phase of calculated transfer coefficients T_Z^{IR} and T_Z^{SF}, and the experimentally observed $\chi^{(2)}_{ZZZ}$. The amplitude and phase of T_Z^{IR} and T_Z^{SF} are normalized and shifted to take the same value of $\chi^{(2)}_{ZZZ}$ at 3100 cm^{-1}. The horizontal axis of T_Z^{SF} is derived from the frequency of sum-frequency light subtracted by the frequency of incident visible light.

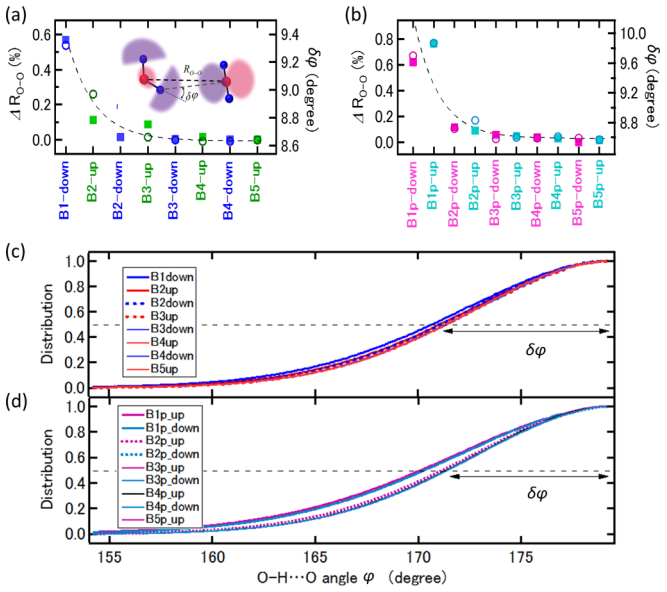

FIG. 11. [(a) and (b)] The half width at half maximum for the distribution of O-H···O angle, $\delta\varphi$ (open circle), and the deviations of $\langle R_{\mathrm{O\text{-}O}}\rangle$ from the bulk value $\langle R^{\mathrm{bulk}}_{\mathrm{O\text{-}O}}\rangle$, $\Delta R_{\mathrm{O\text{-}O}} \equiv (\langle R_{\mathrm{O\text{-}O}}\rangle - \langle R^{\mathrm{bulk}}_{\mathrm{O\text{-}O}}\rangle)/\langle R^{\mathrm{bulk}}_{\mathrm{O\text{-}O}}\rangle$ (filled square) for various interbilayer (a) and intrabilayer (b) hydrogen bonds. [(c) and (d)] Probability distribution of O-H···O angle φ for interbilayer (c) and intrabilayer (d) hydrogen bonds normalized by the value at $\varphi = 180°$. The definitions of Bn-up, Bn-down, Bnp-up, and Bnp-down are given in Fig. 4(a).

In comparison with the $\chi^{(2)}_{\mathrm{eff},PPP}$ spectrum, the frequency dependence of the transfer coefficients is considerably small. Therefore the $\chi^{(2)}_{\mathrm{eff},PPP}$ spectrum is dominated by vibrational response of $\chi^{(2)}_{R,ZZZ}$. Thus, we can extract $\chi^{(2)}_{R,ZZZ}$ from $\chi^{(2)}_{\mathrm{eff},PPP}$ as described in Appendix A. Because the refractive indices of HDO ice (n_1) used here are constituted by a linear combination of those of H_2O and D_2O ice Ih with a D_2O/H_2O ratio of 3.4, the strict spectral shape of T_Z^{IR} would be different from that of Fig. 10. Note that the discussion in Appendixes A and B for H-diluted HDO ice is only based on the fact that the IR wavenumber dependence of the $|T_Z^{\mathrm{IR}}|$ and ArgT_Z^{IR} is negligibly small compared with that of the $\chi^{(2)}_{R,ZZZ}$.

APPENDIX C: CONTRIBUTION TO SFG SPECTRUM OTHER THAN DIPOLE TRANSITION AND ESTIMATION OF SFG ACTIVE REGION AT ICE SURFACE

In addition to the electric dipole transition, an electric quadrupole transition would also contribute to the SFG spectrum [54,111–114]; thus $\chi^{(2)}$ is expressed as

$$\chi^{(2)} = \chi^{ID} + \chi^{IQI} + \chi^{IQB} + \chi^{B}. \tag{C1}$$

where χ^{ID} is derived from the electric dipole transition at ice surface (Ref. [86], Sec. 3), χ^{IQI} and χ^{IQB}O riginate from the quadrupole transition at ice surface due to drastic change in refractive indices and a local electric field within surface few bilayers, and χ^{B} originate from the quadrupole transition due to a large number of water molecules in bulk. χ^{IQI} and χ^{IQB} depend only on surface and bulk properties, respectively [54,114].

We discuss the contributions of four components in Eq. (C1) to the observed SFG spectrum. Note that the coherent length, which is limited by a wave-vector mismatch, of our SFG measurement is calculated to be 4.7 μm [115] in our experimental set up. Within the coherent length, the intensity of χ^{B} should in principle increase with film thickness, because χ^{B} is derived from water molecules in bulk ice. However, we observed that both the intensity and line shape of SFG spectra do not change during the layer-by-layer growth of ice-Ih films from 100 BL to 170 BL on Rh(111) [Fig. 2(a)]. This result clearly indicates that the χ^{B} term little contributes to the observed SFG spectrum, in good agreement with the theoretical prediction for H_2O ice [54]. In ref. [54], it was also reported that the χ^{IQI} term is negligibly small compared with the χ^{ID} term at ice surface.

To evaluate the contribution of χ^{ID} and χ^{IQB} to the observed SFG spectrum, we deposited D_2O ice on an HDO crystalline ice film with sufficient thickness, and observed D_2O-ice thickness dependence of SFG intensity; the intensity of the SFG spectrum at hydrogen-bonded OH-stretch region significantly diminishes upon the deposition of 1 bilayers of D_2O ice [Fig. 2(b)]. Note that the origin of the χ^{ID} term of the OH-stretch band is the structural relaxation at subsurface as discussed in the main text. Therefore the χ^{ID} term of hydrogen-bonded OH-stretch band would be diminished by D_2O-ice deposition on the HDO ice surface, because the inherently relaxed structure of HDO molecules near the surface (Figs. 5, 11, and 12) is converted to the bulk structure where both the interbilayer distance and librational fluctuation of OH oscillators do not depend on the orientation of OH oscillator as the B4-down and B5-up configurations shown in Fig. 5(b). In contrast, the χ^{IQB} term in the OH-stretch region is derived from the bulk property of the HDO ice film [54,114], and thus D_2O-ice deposition would not affect the χ^{IQB} term in the OH-stretch region. Therefore our experimental result [Fig. 2(b)] clearly indicates that the observed SFG signal is dominated by the χ^{ID} term

$$\chi^{(2)} \approx \chi^{ID}, \tag{C2}$$

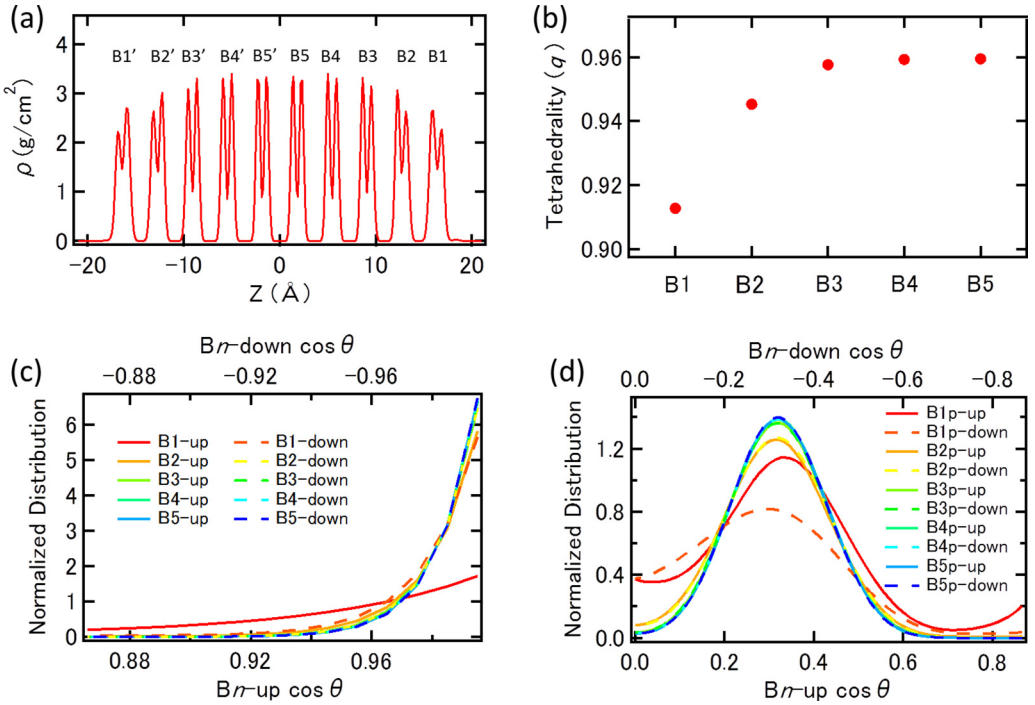

FIG. 12. (a) Density profile of the center of mass for water molecules (∼ position of oxygen atoms). (b) Tetrahedrality at each bilayer. [(c) and (d)] Area normalized probability distribution of tilt angle θ with respect to the c axis for interbilayer OH oscillators (c) and intrabilayer OH oscillators (d). Note that the B1-up OH oscillators do not form H-bond with other molecules and are freely dangling at the topmost surface.

and the SFG signal is derived from the topmost 2–3 bilayers of ice surface, in good agreement with our calculations (Figs. 4 and 5).

APPENDIX D: STRUCTURE OF ICE SURFACE CALCULATED BY MD SIMULATION

Figures 11 and 12 show the results of structure parameters of ice Ih(0001) at 130 K. In Fig. 12(b), the order parameter, "tetrahedrality," is also plotted to quantify the local tetrahedral order in the first solvation shell around a water molecule in each bilayer. For surface of ice, the tetrahedrality q_i around a molecule i has been defined in the following formula [52],

$$q_{\mathrm{i}} = 1 - \frac{9}{2N_i(N_i-1)} \sum_{j=1}^{3} \sum_{k=j+1}^{4} \left(\cos\psi_{jk} + \frac{1}{3}\right)^2, \qquad \text{(D1)}$$

where N_i is the coordination number of ith molecule, j and k denote the water molecules in the first solvation shell around the center molecule i, $\cos\psi_{jk} = \hat{r}_{\mathrm{O}j} \cdot \hat{r}_{\mathrm{O}k}$, where $\hat{r}_{\mathrm{O}j}$ is the unit vector pointing from oxygen of the center molecule i to that of the molecule j. We note that for complete tetrahedron $\psi_{jk} = \cos^{-1}(-1/3) = 109.47^\circ$ results in $\langle q_i \rangle = 1$. In contrast, $\langle q_i \rangle = 0$ for completely random structures like water molecules in gas phase.

[1] V. F. Petrenko and R. W. Whitworth, *Physics of Ice* (Oxford University Press, New York, NY, 1999).

[2] Y. Li and G. A. Somorjai, Surface Premelting of Ice, J. Phys. Chem. C **111**, 9631 (2007).

[3] A.-M. Kietzig, S. G. Hatzikiriakos, and P. Englezos, Physics of ice friction, J. Appl. Phys. **107**, 081101 (2010).

[4] Y. Huang *et al.*, Hydrogen-bond relaxation dynamics: Resolving mysteries of water ice, Coord. Chem. Rev. **285**, 109 (2015).

[5] C. Hoose, J. E. Kristjánsson, J.-P. Chen, and A. Hazra, A classical-theory-based parameterization of heterogeneous ice nucleation by mineral dust, soot, and biological particles in a global climate model, J. Atmos. Sci. **67**, 2483 (2010).

[6] T. Hama, A. Kouchi, and N. Watanabe, Statistical ortho-to-para ratio of water desorbed from ice at 10 kelvin, Science **351**, 65 (2016).

[7] C. Saunders, Charge separation mechanisms in clouds, Space Sci. Rev. **137**, 335 (2008).

[8] D. W. J. Thompson *et al.*, Signatures of the Antarctic ozone hole in Southern Hemisphere surface climate change, Nat. Geosci. **4**, 741 (2011).

[9] N. Watanabe and A. Kouchi, Ice surface reactions: A key to chemical evolution in space, Prog. Surf. Sci. **83**, 439 (2008).

[10] T. Sugimoto and K. Fukutani, Electric-field-induced nuclear-spin flips mediated by enhanced spin–orbit coupling, Nat. Phys. **7**, 307 (2011).

[11] S. Kim, E. Park, and H. Kang, Segregation of hydroxide ions to an ice surface, J. Chem. Phys. **135**, 074703 (2011).

[12] Z. Sun, D. Pan, L. Xu, and E. Wang, Role of proton ordering in adsorption preference of polar molecule on ice surface, Proc. Natl. Acad. Sci. U.S.A. **109**, 13177 (2012).

[13] M. Watkins *et al.*, Large variation of vacancy formation energies in the surface of crystalline ice, Nat. Mater. **10**, 794 (2011).

[14] I. E. L. Stephens *et al.*, Tuning the activity of Pt(111) for oxygen electroreduction by subsurface alloying, J. Am. Chem. Soc. **133**, 5485 (2011).

[15] I. Beinik, M. Hellström, T. N. Jensen, P. Broqvist, and J. V Lauritsen, Enhanced wetting of Cu on ZnO by migration of subsurface oxygen vacancies, Nat. Commun. **6**, 8845 (2015).

[16] D. M. Herlihy *et al.*, Detecting the oxyl radical of photocatalytic water oxidation at an n-$SrTiO_3$/aqueous interface through its subsurface vibration, Nat. Chem. **8**, 549 (2016).

[17] M. Matsumoto, K. Fukutani, and T. Okano, Dynamical LEED analyses of the clean and the NO-adsorbed Ir(111) surface, Surf. Sci. **606**, 1489 (2012).

[18] G. Zhu, G. Radtke, and G. A. Botton, Bonding and structure of a reconstructed (001) surface of $SrTiO_3$ from TEM, Nature (London) **490**, 384 (2012).

[19] H. Morisaki *et al.*, Large surface relaxation in the organic semiconductor tetracene, Nat. Commun. **5**, 5400 (2014).

[20] J. Vogt and H. Weiss, The structure of NaCl(100) and KCl(100) single crystal surfaces: A tensor low energy electron diffraction analysis, Surf. Sci. **491**, 155 (2001).

[21] J. Harnett, S. Haq, and A. Hodgson, Electron induced restructuring of crystalline ice adsorbed on Pt(111), Surf. Sci. **528**, 15 (2003).

[22] N. G. Petrik and G. A. Kimmel, Electron-stimulated production of molecular hydrogen at the interfaces of amorphous solid water films on Pt(111), J. Chem. Phys. **121**, 3736 (2004).

[23] D. Nordlund *et al.*, Surface structure of thin ice films, Chem. Phys. Lett. **395**, 161 (2004).

[24] P. Parent, C. Laffon, C. Mangeney, F. Bournel, and M. Tronc, Structure of the water ice surface studied by x-ray absorption spectroscopy at the O K-edge, J. Chem. Phys. **117**, 10842 (2002).

[25] I. A. Ryzhkin, Thermodynamics of ice: Not obeying the rules, Nat. Phys. **12**, 996 (2016).

[26] S. T. Bramwell, Spin ice state in frustrated magnetic pyrochlore materials, Science **294**, 1495 (2001).

[27] N. Avidor and W. Allison, Helium diffraction as a probe of structure and proton order on model ice surfaces, J. Phys. Chem. Lett. **7**, 4520 (2016).

[28] A. Glebov, A. P. Graham, A. Menzel, J. P. Toennies, and P. Senet, A helium atom scattering study of the structure and phonon dynamics of the ice surface, J. Chem. Phys. **112**, 11011 (2000).

[29] M. Morgenstern, J. Müller, T. Michely, and G. Comsa, The ice bilayer on Pt(111): Nucleation, structure and melting, Zeitschrift für Phys. Chemie. **198**, 43 (1997).

[30] K. Thürmer and S. Nie, Formation of hexagonal and cubic ice during low-temperature growth, Proc. Natl. Acad. Sci. U.S.A. **110**, 11757 (2013).

[31] N. Materer *et al.*, Molecular surface structure of a low-temperature ice Ih(0001) crystal, J. Phys. Chem. **99**, 6267 (1995).

[32] N. Materer *et al.*, Molecular surface structure of ice(0001): dynamical low-energy electron diffraction, total-energy calculations and molecular dynamics simulations, Surf. Sci. **381**, 190 (1997).

[33] Y. R. Shen, Phase-sensitive sum-frequency spectroscopy, Annu. Rev. Phys. Chem. **64**, 129 (2013).

[34] S. Nihonyanagi, J. A. Mondal, S. Yamaguchi, and T. Tahara, Structure and dynamics of interfacial water studied by heterodyne-detected vibrational sum-frequency generation, Annu. Rev. Phys. Chem. **64**, 579 (2013).

[35] T. Sugimoto, N. Aiga, Y. Otsuki, K. Watanabe, and Y. Matsumoto, Emergent high-Tc ferroelectric ordering of strongly correlated and frustrated protons in a heteroepitaxial ice film, Nat. Phys. **12**, 1063 (2016).

[36] S. Nihonyanagi *et al.*, Accurate determination of complex $\chi^{(2)}$ spectrum of the air/water interface, J. Chem. Phys. **143**, 124707 (2015).

[37] S. Sun *et al.*, Phase reference in phase-sensitive sum-frequency vibrational spectroscopy, J. Chem. Phys. **144**, 244711 (2016).

[38] S. Yamaguchi, Comment on "Phase reference in phase-sensitive sum-frequency vibrational spectroscopy" [J. Chem. Phys. 144, 244711 (2016)], J. Chem. Phys. **145**, 167101 (2016).

[39] S. Nihonyanagi, S. Yamaguchi, and T. Tahara, Water hydrogen bond structure near highly charged interfaces is not like ice, J. Am. Chem. Soc. **132**, 6867 (2010).

[40] X. Wei, P. B. Miranda, and Y. R. Shen, Surface Vibrational Spectroscopic Study of Surface Melting of Ice, Phys. Rev. Lett. **86**, 1554 (2001).

[41] X. Wei, P. B. Miranda, C. Zhang, and Y. R. Shen, Sum-frequency spectroscopic studies of ice interfaces, Phys. Rev. B. **66**, 085401 (2002).

[42] V. Buch *et al.*, Sum frequency generation surface spectra of ice, water, and acid solution investigated by an exciton model, J. Chem. Phys. **127**, 204710 (2007).

[43] H. Groenzin, I. Li, V. Buch, and M. J. Shultz, The single-crystal, basal face of ice I_h investigated with sum frequency generation, J. Chem. Phys. **127**, 214502 (2007).

[44] V. Buch, H. Groenzin, I. Li, M. J. Shultz, and E. Tosatti, Proton order in the ice crystal surface, Proc. Natl. Acad. Sci. U.S.A. **105**, 5969 (2008).

[45] H. Groenzin, I. Li, and M. J. Shultz, Sum-frequency generation: Polarization surface spectroscopy analysis of the vibrational surface modes on the basal face of ice I_h, J. Chem. Phys. **128**, 214510 (2008).

[46] I. Li Barnett, H. Groenzin, and M. J. Shultz, Hydrogen bonding in the hexagonal ice surface, J. Phys. Chem. A. **115**, 6039 (2011).

[47] P. J. Bisson and M. J. Shultz, Hydrogen bonding in the prism face of ice I_h via sum frequency vibrational spectroscopy, J. Phys. Chem. A. **117**, 6116 (2013).

[48] M. A. Sánchez *et al.*, Experimental and theoretical evidence for bilayer-by-bilayer surface melting of crystalline ice, Proc. Natl. Acad. Sci. U.S.A. **114**, 227 (2017).

[49] L. Delzeit, J. P. Devlin, and V. Buch, Structural relaxation rates near the ice surface: Basis for separation of the surface and subsurface spectra, J. Chem. Phys. **107**, 3726 (1997).

[50] L. Shi, S. M. Gruenbaum, and J. L. Skinner, Interpretation of IR and raman line shapes for H_2O and D_2O Ice Ih, J. Phys. Chem. B. **116**, 13821 (2012).

[51] H. Liu, Y. Wang, and J. M. Bowman, Quantum calculations of intramolecular IR spectra of ice models using ab initio potential and dipole moment surfaces, J. Phys. Chem. Lett. **3**, 3671 (2012).

[52] T. Ishiyama, H. Takahashi, and A. Morita, Origin of vibrational spectroscopic response at ice surface, J. Phys. Chem. Lett. **3**, 3001 (2012).

[53] T. Ishiyama and A. Morita, A direct evidence of vibrationally delocalized response at ice surface, J. Chem. Phys. **141**, 18C503 (2014).
[54] Q. Wan and G. Galli, First-Principles Framework to Compute Sum-Frequency Generation Vibrational Spectra of Semiconductors and Insulators, Phys. Rev. Lett. **115**, 246404 (2015).
[55] F. Li and J. L. Skinner, Infrared and Raman line shapes for ice Ih. I. Dilute HOD in H_2O and D_2O, J. Chem. Phys. **132**, 204505 (2010).
[56] H. Liu, Y. Wang, and J. M. Bowman, Local-monomer calculations of the intramolecular IR spectra of the cage and prism isomers of $HOD(D_2O)_5$ and HOD and D_2O Ice Ih, J. Phys. Chem. B. **118**, 14124 (2014).
[57] D. D. Klug, O. Mishima, and E. Whalley, High-density amorphous ice. IV. Raman spectrum of the uncoupled O–H and O–D oscillators, J. Chem. Phys. **86**, 5323 (1987).
[58] D. D. Klug and E. Whalley, The uncoupled O–H stretch in ice VII. The infrared frequency and integrated intensity up to 189 kbar, J. Chem. Phys. **81**, 1220 (1984).
[59] B. Kamb, W. C. Hamilton, S. J. Laplaca, and A. Prakash, Ordered proton configuration in ice II, from single-crystal neutron diffraction, J. Chem. Phys. **55**, 1934 (1971).
[60] A. Beniya, S. Yamamoto, K. Mukai, Y. Yamashita, and J. Yoshinobu, The first layer of water on Rh(111): Microscopic structure and desorption kinetics, J. Chem. Phys. **125**, 054717 (2006).
[61] F. T. Wagner and T. E. Moylan, A comparison between water adsorbed on Rh(111) and Pt(111), with and without predosed oxygen, Surf. Sci. **191**, 121 (1987).
[62] J. Kiss and F. Solymosi, Adsorption of H_2O on clean and on boron-contaminated Rh surfaces, Surf. Sci. **177**, 191 (1986).
[63] J. Meija, Z. Mester, and A. D'Ulivo, Mass spectrometric separation and quantitation of overlapping isotopologues. H_2O/HOD/D_2O and H_2Se/HDSe/D_2Se mixtures, J. Am. Soc. Mass Spectrom. **17**, 1028 (2006).
[64] K. Inoue, K. Watanabe, T. Sugimoto, Y. Matsumoto, and T. Yasuike, Disentangling Multidimensional Nonequilibrium Dynamics of Adsorbates: CO Desorption from Cu(100), Phys. Rev. Lett. **117**, 186101 (2016).
[65] M. Nagao, K. Watanabe, and Y. Matsumoto, Ultrafast vibrational energy transfer in the layers of D_2O and CO on Pt(111) studied with time-resolved sum-frequency-generation spectroscopy, J. Phys. Chem. C. **113**, 11712 (2009).
[66] K. Inoue, K. Watanabe, and Y. Matsumoto, Instantaneous vibrational frequencies of diffusing and desorbing adsorbates: CO/Pt(111), J. Chem. Phys. **137**, 024704 (2012).
[67] K. Watanabe, K. Inoue, I. F. Nakai, and Y. Matsumoto, Nonadiabatic coupling between C-O stretching and Pt substrate electrons enhanced by frustrated mode excitations, Phys. Rev. B. **81**, 241408 (2010).
[68] K. D. Gibson, M. Viste, and S. J. Sibener, The adsorption of water on clean and oxygen predosed Rh(111): Surface templating via (1×1)-O/Rh(111) induces formation of a novel high-density interfacial ice structure, J. Chem. Phys. **112**, 9582 (2000).
[69] A. Beniya *et al.*, The growth process of first water layer and crystalline ice on the Rh(111) surface, J. Chem. Phys. **130**, 034706 (2009).
[70] T. Yamada, H. Okuyama, T. Aruga, and M. Nishijima, Vibrational spectroscopy of crystalline multilayer ice: Surface modes in the intermolecular-vibration region, J. Phys. Chem. B. **107**, 13962 (2003).
[71] M. Mehlhorn and K. Morgenstern, Faceting during the Transformation of Amorphous to Crystalline Ice, Phys. Rev. Lett. **99**, 246101 (2007).
[72] S. Maier, B. A. J. Lechner, G. A. Somorjai, and M. Salmeron, Growth and structure of the first layers of ice on Ru(0001) and Pt(111), J. Am. Chem. Soc. **138**, 3145 (2016).
[73] M. Bockstedte, A. Michl, M. Kolb, M. Mehlhorn, and K. Morgenstern, Incomplete bilayer termination of the ice (0001) surface, J. Phys. Chem. C. **120**, 1097 (2016).
[74] A. Pedersen, K. T. Wikfeldt, L. Karssemeijer, H. Cuppen, and H. Jónsson, Molecular reordering processes on ice (0001) surfaces from long timescale simulations, J. Chem. Phys. **141**, 234706 (2014).
[75] S.-C. Park, K.-H. Jung, and H. Kang, H/D isotopic exchange between water molecules at ice surfaces, J. Chem. Phys. **121**, 2765 (2004).
[76] A. Beniya, K. Mukai, Y. Yamashita, and J. Yoshinobu, Coverage-dependent sticking probability and desorption kinetics of water molecules on Rh(111), J. Chem. Phys. **129**, 016101 (2008).
[77] R. S. Smith, J. Matthiesen, J. Knox, and B. D. Kay, Crystallization kinetics and excess free energy of H_2O and D_2O nanoscale films of amorphous solid water, J. Phys. Chem. A. **115**, 5908 (2011).
[78] J. P. Devlin and V. Buch, Surface of ice as viewed from combined spectroscopic and computer modeling studies, J. Phys. Chem. **99**, 16534 (1995).
[79] J. L. F. Abascal, E. Sanz, R. García Fernández, and C. Vega, A potential model for the study of ices and amorphous water: TIP4P/Ice, J. Chem. Phys. **122**, 234511 (2005).
[80] V. Buch, P. Sandler, and J. Sadlej, Simulations of H_2O solid, liquid, and clusters, with an emphasis on ferroelectric ordering transition in hexagonal ice, J. Phys. Chem. B. **102**, 8641 (1998).
[81] M. Parrinello, Polymorphic transitions in single crystals: A new molecular dynamics method, J. Appl. Phys. **52**, 7182 (1981).
[82] S. Nosé, A unified formulation of the constant temperature molecular dynamics methods, J. Chem. Phys. **81**, 511 (1984).
[83] W. G. Hoover, Canonical dynamics: Equilibrium phase-space distributions, Phys. Rev. A. **31**, 1695 (1985).
[84] B. Hess, C. Kutzner, D. van der Spoel, and E. Lindahl, GROMACS 4: Algorithms for highly efficient, load-balanced, and scalable molecular simulation, J. Chem. Theory Comput. **4**, 435 (2008).
[85] T. Ishiyama and A. Morita, Analysis of anisotropic local field in sum frequency generation spectroscopy with the charge response kernel water model, J. Chem. Phys. **131**, 244714 (2009).
[86] See Supplemental Material at http://link.aps.org/supplemental/10.1103/PhysRevB.96.115405 for the effect of isotope ratio on the width of the SFG spectra, defnition of the QM/MM spectra of hydrogen-bonded local OH oscillators and basic theoretical back ground of SFG spectroscopy, which includes Refs. [116–125].
[87] T. Ishiyama and A. Morita, Molecular dynamics study of gas−liquid aqueous sodium halide interfaces. I. Flexible and polarizable molecular modeling and interfacial properties, J. Phys. Chem. C **111**, 721 (2007).

[88] A. Morita and T. Ishiyama, Recent progress in theoretical analysis of vibrational sum frequency generation spectroscopy, Phys. Chem. Chem. Phys. **10**, 5801 (2008).
[89] T. Ishiyama, H. Takahashi, and A. Morita, Molecular dynamics simulations of surface-specific bonding of the hydrogen network of water: A solution to the low sum-frequency spectra, Phys. Rev. B. **86**, 035408 (2012).
[90] Y. Yamaguchi, M. Frisch, J. Gaw, H. F. Schaefer, and J. S. Binkley, Analytic evaluation and basis set dependence of intensities of infrared spectra, J. Chem. Phys. **84**, 2262 (1986).
[91] J. R. Cheeseman and M. J. Frisch, Basis set dependence of vibrational raman and raman optical activity intensities, J. Chem. Theory Comput. **7**, 3323 (2011).
[92] A. Morita and S. Kato, An ab initio analysis of medium perturbation on molecular polarizabilities, J. Chem. Phys. **110**, 11987 (1999).
[93] W. H. Thompson and J. T. Hynes, Frequency shifts in the hydrogen-bonded oh stretch in halide−water clusters. The importance of charge transfer, J. Am. Chem. Soc. **122**, 6278 (2000).
[94] A. E. Reed, L. A. Curtiss, and F. Weinhold, Intermolecular interactions from a natural bond orbital, donor-acceptor viewpoint, Chem. Rev. **88**, 899 (1988).
[95] B. A. Zilles and W. B. Person, Interpretation of infrared intensity changes on molecular complex formation. I. Water dimer, J. Chem. Phys. **79**, 65 (1983).
[96] K. Ohno, M. Okimura, N. Akai, and Y. Katsumoto, The effect of cooperative hydrogen bonding on the OH stretching-band shift for water clusters studied by matrix-isolation infrared spectroscopy and density functional theory, Phys. Chem. Chem. Phys. **7**, 3005 (2005).
[97] C. J. Tainter and J. L. Skinner, The water hexamer: Three-body interactions, structures, energetics, and OH-stretch spectroscopy at finite temperature, J. Chem. Phys. **137**, 104304 (2012).
[98] P. A. F. P. Moreira and M. de Koning, Nuclear quantum fluctuations in ice I_h, Phys. Chem. Chem. Phys. **17**, 24716 (2015).
[99] K. R. Wilson *et al.*, Surface relaxation in liquid water and methanol studied by x-ray absorption spectroscopy, J. Chem. Phys. **117**, 7738 (2002).
[100] F. Li and J. L. Skinner, Infrared and Raman line shapes for ice Ih. II. H_2O and D_2O, J. Chem. Phys. **133**, 244504 (2010).
[101] J. L. F. Da Silva, C. Stampfl, and M. Scheffler, Converged properties of clean metal surfaces by all-electron first-principles calculations, Surf. Sci. **600**, 703 (2006).
[102] N. H. Fletcher, Reconstruction of ice crystal surfaces at low temperatures, Philos. Mag. Part B. **66**, 109 (1992).
[103] D. Pan *et al.*, Surface Energy and Surface Proton Order of Ice I*h*, Phys. Rev. Lett. **101**, 155703 (2008).
[104] W. J. Smit *et al.*, Observation and identification of a new OH stretch vibrational band at the surface of ice, J. Phys. Chem. Lett. **8**, 3656 (2017).
[105] S. Yamaguchi, K. Shiratori, A. Morita, and T. Tahara, Electric quadrupole contribution to the nonresonant background of sum frequency generation at air/liquid interfaces, J. Chem. Phys. **134**, 184705 (2011).
[106] A. G. Lambert, P. B. Davies, and D. J. Neivandt, Implementing the theory of sum frequency generation vibrational spectroscopy: A tutorial review, Appl. Spectrosc. Rev. **40**, 103 (2005).
[107] E. D. Palik, *Handbook of Optical Constants of Solids* (Academic press, Orlando, 1985).
[108] D. B. O'Brien and A. M. Massari, Modeling multilayer thin film interference effects in interface-specific coherent nonlinear optical spectroscopies, J. Opt. Soc. Am. B. **30**, 1503 (2013).
[109] X. Zhuang, P. B. Miranda, D. Kim, and Y. R. Shen, Mapping molecular orientation and conformation at interfaces by surface nonlinear optics, Phys. Rev. B. **59**, 12632 (1999).
[110] A. Myalitsin, S. Urashima, S. Nihonyanagi, S. Yamaguchi, and T. Tahara, Water structure at the buried silica/aqueous interface studied by heterodyne-detected vibrational sum-frequency generation, J. Phys. Chem. C. **120**, 9357 (2016).
[111] P. Guyot-Sionnest and Y. R. Shen, Bulk contribution in surface second-harmonic generation, Phys. Rev. B. **38**, 7985 (1988).
[112] K. Shiratori, S. Yamaguchi, T. Tahara, and A. Morita, Computational analysis of the quadrupole contribution in the second-harmonic generation spectroscopy for the water/vapor interface, J. Chem. Phys. **138**, 064704 (2013).
[113] K. Matsuzaki, S. Nihonyanagi, S. Yamaguchi, T. Nagata, and T. Tahara, Vibrational sum frequency generation by the quadrupolar mechanism at the nonpolar benzene/air interface, J. Phys. Chem. Lett. **4**, 1654 (2013).
[114] K. Shiratori and A. Morita, Theory of quadrupole contributions from interface and bulk in second-order optical processes, Bull. Chem. Soc. Jpn. **85**, 1061 (2012).
[115] V. Ostroverkhov, G. A. Waychunas, and Y. R. Shen, New Information on Water Interfacial Structure Revealed by Phase-Sensitive Surface Spectroscopy, Phys. Rev. Lett. **94**, 046102 (2005).
[116] T. A. Ford and M. Falk, Hydrogen bonding in water and ice, Can. J. Chem. **46**, 3579 (1968).
[117] S.-I. Ikawa and S. Maeda, Infrared intensities of the stretching and librational bands of H_2O, D_2O, and HDO in solids, Spectrochim. Acta. A **24**, 655 (1968).
[118] D. F. Hornig, H. F. White, and F. P. Reding, The infrared spectra of crystalline H_2O, D_2O and HDO, Spectrochim. Acta. **12**, 338 (1958).
[119] J. R. Scherer and R. G. Snyder, Raman intensities of single crystal ice Ih, J. Chem. Phys. **67**, 4794 (1977).
[120] C. S. Tian and Y. R. Shen, Recent progress on sum-frequency spectroscopy, Surf. Sci. Rep. **69**, 105 (2014).
[121] M. Bonn, Y. Nagata, and E. H. G. Backus, Molecular structure and dynamics of water at the water-air interface studied with surface-specific vibrational spectroscopy, Angew. Chemie Int. Ed. **54**, 5560 (2015).
[122] R. W. Boyd, *Nonlinear Optics*, 3rd ed. (Academic Press, New York, 2008).
[123] Q. Du, R. Superfine, E. Freysz, and Y. R. Shen, Vibrational Spectroscopy Of Water At The Vapor/Water Interface, Phys. Rev. Lett. **70**, 2313 (1993).
[124] K. C. Chou, S. Westerberg, Y. R. Shen, P. N. Ross, and G. A. Somorjai, Probing the charge-transfer state of CO on Pt(111) by two-dimensional infrared-visible sum frequency generation spectroscopy, Phys. Rev. B. **69**, 153413 (2004).
[125] W. F. Murphy, The rovibrational Raman spectrum of water vapour v_1 and v_3, Mol. Phys. **36**, 727 (1978).